

A Preliminary Study of Wear in the Solid-Armature Railgun

J. Powell and A. Zielinski

*Institute for Advanced Technology
The University of Texas at Austin*

December 1997

IAT.R 0156

Approved for public release; distribution unlimited. DTIC QUALITY INSPECTED 4

19980316 038

19980326 016

The views, opinions, and/or findings contained in this report are those of the author(s) and should not be construed as an official Department of the Army position, policy, or decision, unless so designated by other documentation.

REPORT DOCUMENTATION PAGE

Form Approved
OMB NO. 0704-0188

Public reporting burden for this collection of information is estimated to average 1 hour per response, including the time for reviewing instructions, searching existing data sources, gathering and maintaining the data needed, and completing and reviewing the collection of information. Send comments regarding this burden estimate or any other aspect of this collection of information, including suggestions for reducing this burden, to Washington Headquarters Services, Directorate for Information Operations and Reports, 1215 Jefferson Davis Highway, Suite 1204, Arlington, VA 22202-4302, and to the Office of Management and Budget, Paperwork Reduction Project (0704-0188), Washington, DC 20503.

1. AGENCY USE ONLY (Leave blank)	2. REPORT DATE December 1997	3. REPORT TYPE AND DATES COVERED Technical Report	
4. TITLE AND SUBTITLE A Preliminary Study of Wear in the Solid-Armature Railgun		5. FUNDING NUMBERS Contract # DAAA21-93-C-0101	
6. AUTHOR(S) J. Powell and A. Zielinski			
7. PERFORMING ORGANIZATION NAME(S) AND ADDRESS(ES) Institute for Advanced Technology The University of Texas at Austin 4030-2 W. Braker Lane, #200 Austin, TX 78759		8. PERFORMING ORGANIZATION REPORT NUMBER IAT.R 0156	
9. SPONSORING / MONITORING AGENCY NAME(S) AND ADDRESS(ES) U.S. Army Research Laboratory ATTN: AMSRL-WT-T Aberdeen Proving Ground, MD 21005-5066		10. SPONSORING / MONITORING AGENCY REPORT NUMBER	
11. SUPPLEMENTARY NOTES The view, opinions and/or findings contained in this report are those of the author(s) and should not be considered as an official Department of the Army position, policy, or decision, unless so designated by other documentation.			
12a. DISTRIBUTION / AVAILABILITY STATEMENT Approved for public release; distribution unlimited.		12b. DISTRIBUTION CODE A	
13. ABSTRACT (Maximum 200 words) A model previously developed to investigate current and heat transport in solid-armature railguns is extended. The 2-dimensional model involves the numerical solution of coupled Maxwell and heat-transport equations in both the armature and rails of the railgun. The principal extensions include the development of a general transformation which maps an armature of fairly arbitrary shape into a rectangular computational region, and the inclusion of melting within the appropriate governing equations. Two specific applications of the theory are then discussed: analysis of an armature under experimental study at the Army Research Laboratory and preliminary calculations concerning the entrainment of armature material on the surfaces of the rails.			
14. SUBJECT TERMS solid-armature railguns, armature melting, 2-D armature model, railgun modeling, armature wear		15. NUMBER OF PAGES 46	
		16. PRICE CODE	
17. SECURITY CLASSIFICATION OF REPORT Unclassified	18. SECURITY CLASSIFICATION OF THIS PAGE Unclassified	19. SECURITY CLASSIFICATION OF ABSTRACT Unclassified	20. LIMITATION OF ABSTRACT UL

Table of Contents

Introduction.....	3
Model and Formalism.....	7
Governing Equations	7
Boundary Conditions.....	10
Representation of the Heat Absorbed During Melting.....	12
Transformed Coordinates.....	13
Analysis of Scaled MCA 1.0.5.....	17
Geometry and Transformation Coordinates.....	18
Input Current Versus Time.....	21
Results of Calculations.....	22
Entrainment of Melted Armature Material on the Rails.....	30
Summary and Conclusions.....	35
Acknowledgments.....	37
References.....	37
Appendix A: Transformation Metrics.....	39
Appendix B: Material Properties	43
Distribution List.....	45

List of Figures

Figure 1. Schematic Diagram Depicting the Operation of a Railgun	4
Figure 2. Schematic Diagram for Rail-Armature Model Calculations.....	8
Figure 3. Function, $F(T)$, Depicting Amount of Melted Material Formed Per..... Unit Rise in Temperature	13
Figure 4. Rectangular Grid for the Computational Domain of the Armature.....	18
Figure 5. Grid for (a) the Physical Domain of the Armature; and (b) the Rails.....	20
Figure 6. Time Dependence of (a) the Current Per Unit Rail Height and (b) the Velocity	22
Figure 7. Lines of Constant Induction within the Armature at $400\ \mu\text{s}$	24
Figure 8. Isotherms within the Armature at $400\ \mu\text{s}$	25
Figure 9. Isotherms within the Armature at $1100\ \mu\text{s}$	26
Figure 10. Temperature Versus x at Constant Values of y : A, Just Inside the Armature ($y = 7.325\ \text{mm}$); I, Along the Interface ($y = 7.5\ \text{mm}$); R, Just Inside the Rails ($y = 7.684\ \text{mm}$)	27
Figure 11. Measured Muzzle Voltage Versus Time.....	28
Figure 12. Flash X-ray Images of Armature Downrange of Launcher	29

A Preliminary Study of Wear in the Solid-Armature Railgun

John D. Powell

Alexander E. Zielinski

Preface

A model previously developed to investigate current and heat transport in solid-armature railguns is extended. The model is two dimensional and involves the numerical solution of coupled Maxwell and heat-transport equations in both the armature and rails of the railgun. The principal extensions include the development of a general transformation which maps an armature of fairly arbitrary shape into a rectangular computational region, and the inclusion of melting within the appropriate governing equations. The transformation is found to facilitate greatly the numerical solution of the problem for complicated armatures. Two specific applications of the theory are then discussed. The first application involves the analysis of an armature under experimental study at the Army Research Laboratory. For this case, temperature and induction-field profiles are calculated within the rails and armature as functions of both space and time, and the physical reasons for the behavior observed are discussed. Some recent experimental data which indicate the performance of the armature are also presented. The second application involves some preliminary calculations concerning the entrainment of armature material on the surfaces of the rails. An estimate of the velocity with which the melt surface progresses through the armature is obtained, and the results are compared with results from a simpler, limiting-case analytic model. Possible reasons for the discrepancy in the two results are discussed and some suggestions for improving the calculations noted.

1. INTRODUCTION

In recent work, we have developed a two-dimensional model for investigating the diffusion of current and heat in a solid-armature railgun. The model has subsequently been employed to study various armatures subjected to various launch conditions. The most detailed investigations have been for a simple railgun used with a "U-shaped" armature (Powell, Walbert, and Zielinski 1993) and, later, for an augmented railgun used with the armature developed for the Cannon-Caliber Electromagnetic Gun Program (Powell and Zielinski 1995a, 1995b). It has been our view that these types of studies are important in order to guide the design of armatures and projectiles, in order to determine the limits under which these launchers can operate, and ultimately in order to study the dynamics of the armature and gun tube.

A schematic diagram showing a cross section of a typical railgun with a simple rectangular armature is shown in Figure 1. The two dimensions depicted, namely, the direction of acceleration and the direction along the rail separation, are the dimensions actually treated in the model calculations. The rails and armature are assumed to be infinitely extended out of the page. Current flows in the direction indicated by the arrows and produces a magnetic induction field that points outward in the inner bore of the gun. This field interacts with the current to produce a Lorentz or $\vec{J} \times \vec{B}$ force that accelerates the armature and projectile down the barrel. Initially, the current flows along the inner surfaces of the conductors and later diffuses into the interior. The intent of the calculations is to determine this time-dependent diffusion and resulting ohmic heating in both the rails and armature.

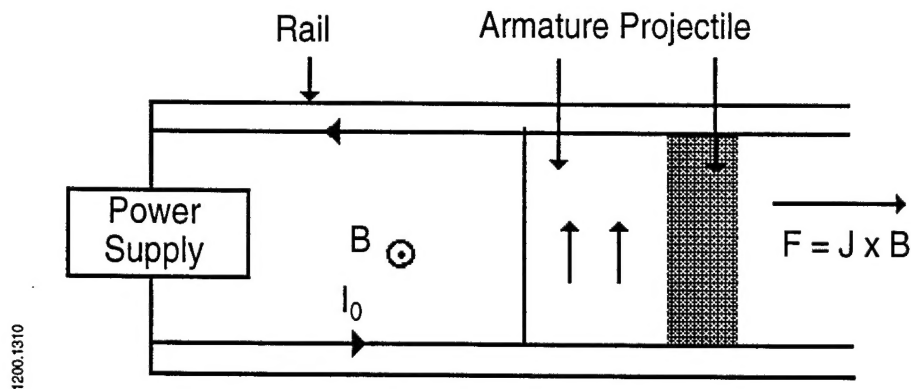


Figure 1. Schematic Diagram Depicting the Operation of a Railgun.

Models similar to that under study here have been investigated in the past by others. A fairly extensive discussion of previous work has been given earlier (Powell, Walbert, and Zielinski 1993) and here we indicate only the most closely related studies. The earliest comprehensive treatment of the two-dimensional problem was provided by Long (1986). He first considered only the electrodynamics problem in the steady state and without ohmic heating, and obtained a complete analytical solution in terms of infinite series. This work provided considerable insight into the problems that might be expected as the velocity of the projectile increased. Long (1987) later extended the calculations in graduate-thesis work to a finite-element solution which included time-dependent effects, resistive heating, and temperature-dependent properties. More recently, finite-element models have been extended to three dimensions by Rodger and coworkers (Rodger, Leonard, Eastman, and Atkinson 1989; Rodger, Leonard, and Eastman 1991; Rodger and Leonard 1991) and by Hsieh (1994). The model developed by Hsieh, known as EMAP3D, has been under particularly active investigation in the last few years and holds considerable promise of elucidating many outstanding problems in solid-armature railgun dynamics.

In the present work, we will be interested in providing a number of extensions to our existing two-dimensional model. First, we will include the latent heat of fusion in the energy equation as well as material properties for the liquid phase. In our earlier work, melting was not accounted for and the temperature was simply allowed to rise beyond the melt temperature with no change in phase assumed. Melting will be accounted for only in the armature which is assumed to be aluminum, and not in the rails which are assumed to be copper. Our calculations have demonstrated that temperatures within the rails remain sufficiently low that melting does not occur under experimental conditions of interest. It would be possible and not particularly difficult to treat melting in the rails as well as to consider other armature and rail materials in the future if such considerations are warranted.

The second extension to the model that we provide is the development of a transformation that maps an armature of fairly general shape into a rectangular region. The governing equations are then solved in this reasonably simple rectangular space. The use of transformed coordinates has been found to simplify vastly the study of armatures with complicated geometry. In particular, the technique is extremely flexible, permits simple specification of boundary conditions, and provides an easy method for grid control.

Third, we will apply our newly developed model to analyze an armature recently investigated experimentally at the Army Research Laboratory (Zielinski and Le 1996). The armature is similar to the MCA 1.0.5 version (Price and Yun 1995) studied extensively at the Institute for Advanced Technology, but is scaled down to be suitable for a 15 mm, rather than a 25 mm, square-bore launcher. We have actually tested the model on a number of other armatures, both simple and reasonably complicated, but will confine most of our discussion to this one specific case. This choice was made primarily because it represents an armature having fairly complicated geometry, amenable to study with the model, and because we have planned to attempt experimental measurements of the temperature on the surface of this armature. We believe that these measurements, if possible, will provide a useful opportunity to compare theoretical and experimental results, especially with regard to current distribution. We will also

discuss briefly some of the existing experimental data for this armature, although detailed comparisons of experiment and calculations are not feasible at this time.

Finally, we will discuss some preliminary work that we have done on the problem of armature melting with subsequent entrainment on the rail surface. There has been some speculation in the past that this sort of behavior may be a principal reason that solid-armature contacts fail at high velocities. Some quantitative analysis of the problem has been conducted by Parks (1990) and by Woods (1996), albeit with rather simple models, and it is timely to undertake more complicated calculations. Our discussion of this problem will be largely qualitative and to some extent speculative since our calculations at this time have been limited. We intend to report more details in a later report when the specific extensions discussed in Section 4 have been carried out.

Before progressing to the calculations, we should point out that there are well-known problems with the use of two-dimensional, infinite-rail height models to analyze real armatures under specific experimental conditions. The principal problem is that two-dimensional models are known to overestimate substantially the magnitude of the in-bore induction fields and the acceleration imparted to the armature. Furthermore, at early times, current that is localized near the back surface of the armature tends to overestimate significantly the effects of ohmic heating. Batteh (1984) has pointed out that some problems can be ameliorated by use of an effective value of the magnetic permeability and, in a complicated calculation, has worked out the appropriate value. This technique works fairly well for steady-state problems, but cannot be expected to apply in the transient case; it will, for example, predict incorrectly the rate at which fields diffuse throughout the armature. In an effort not to overestimate both the Lorentz forces and ohmic heating at early times, we have in the MCA 1.0.5 calculations elected to scale the current down from the actual experimental value to a value that gives the correct acceleration for a real, two-dimensional railgun. This scaling is also not entirely satisfactory since it will underestimate steady-state ohmic heating for that armature. As a consequence, only a qualitative comparison of experimental and theoretical results can be made. The manner in which the scaling is performed will be discussed in more detail subsequently.

There are, however, some advantages in the use of two-dimensional models. These models do contain most of the important physics, and their relative computational simplicity makes the study of those phenomena much easier than in the more realistic three-dimensional calculations. Consequently, it has been our view that two-dimensional models should be employed to study various physical effects, such as interface dynamics, phase changes, and the velocity skin effect. The ultimate goal, however, must be to include the information learned in the more predictive three-dimensional studies.

The organization of this report is as follows. In Section 2, we describe the model in more detail and develop the general formalism and governing equations. Section 3 contains the analysis of the scaled MCA 1.0.5 armature and a discussion of the existing experimental data. In Section 4, we present a qualitative discussion of the rail-entrainment problem, indicate what our present analysis has shown, and suggest what needs to be studied further. Finally, Section 5 contains some general discussion and conclusions.

2. MODEL AND FORMALISM

2.1 Governing Equations. The configuration to be considered is shown schematically in Figure 2. As in previous work, it is convenient to perform calculations in a frame of reference in which the armature is fixed in space and the rails move "backward" with velocity $-v_p$, where v_p is the projectile velocity. As shown in the figure, the plane $x = 0$ is chosen to pass through the trailing edge of the rail-armature interface, whereas the plane $x = \ell_a$ passes through the leading edge. We restrict ourselves to situations in which the armature is symmetric about the line $y = 0$ and thus perform the calculations for only positive values of y . The rails and armature are assumed to be infinitely extended in the z direction to accord with the assumption that the model is two dimensional.

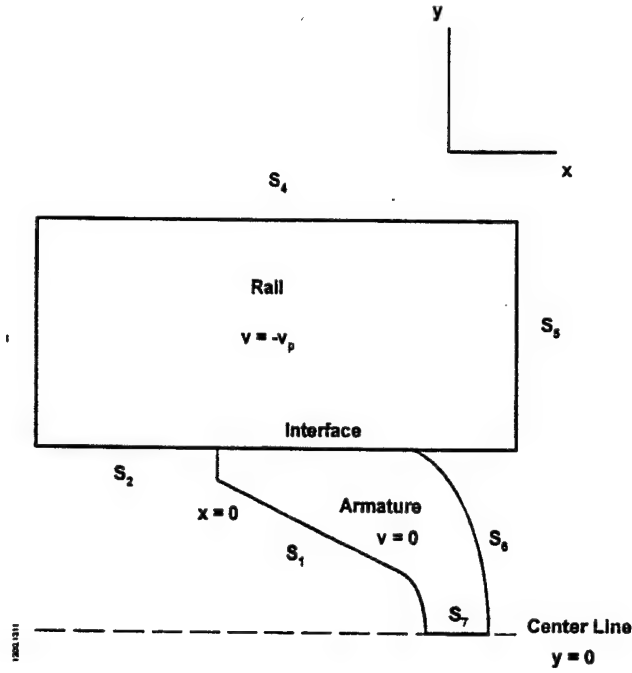


Figure 2. Schematic Diagram for Rail-Armature Model Calculations.

The basic equations that must be solved consist of Maxwell's equations as well as the appropriate energy-transport equation. Let, \vec{J} , \vec{B} , and \vec{E} be the current density, the magnetic induction, and the electric-field intensity. Let μ , κ , σ , and C be the magnetic permeability, the thermal conductivity, the electrical conductivity, and the specific heat. Finally, let T , ρ , and v be the temperature, density, and material velocity at any point in the rail-armature system. The governing Maxwell equations can then be written

$$\nabla \times \vec{E} = -\frac{\partial \vec{B}}{\partial t}, \quad (1)$$

$$\nabla \times \vec{B} = \mu \vec{J}, \quad (2)$$

and

$$\vec{J} = \sigma(\vec{E} + \vec{v} \times \vec{B}). \quad (3)$$

As is customary in these types of calculations, we have neglected the displacement current in equation (1). Such an approximation can be shown to be valid provided the velocity v is small compared to the light speed c , and provided the time scale t_s of the problem satisfies the condition $t_s \gg (\mu\sigma c^2)$. Both these conditions are very easily satisfied for rail-launcher problems.

We now observe that for the infinite rail-height geometry discussed above, we must have $\vec{B} = B\hat{a}_z$ and that J_z and E_z both vanish. Furthermore there can be no z dependence in any of the physical variables. Making use of these observations, we then find that equations (1)-(3) can be uncoupled to produce a single partial differential equation which governs the convection and diffusion of the magnetic induction. The equation is

$$\mu\sigma \frac{\partial B}{\partial t} = \frac{\partial^2 B}{\partial x^2} + \frac{\partial^2 B}{\partial y^2} - \mu\sigma v \frac{\partial B}{\partial x} - \frac{1}{\sigma} \frac{\partial \sigma}{\partial T} \frac{\partial T}{\partial x} \frac{\partial B}{\partial x} - \frac{1}{\sigma} \frac{\partial \sigma}{\partial T} \frac{\partial T}{\partial y} \frac{\partial B}{\partial y}. \quad (4)$$

In obtaining this result, we have assumed that σ depends on position only through the temperature T .

A similar assumption concerning κ and C allows us to write for the energy-transport equation the result

$$\rho C \frac{\partial T}{\partial t} + \rho C v \frac{\partial T}{\partial x} = \kappa \frac{\partial^2 T}{\partial x^2} + \kappa \frac{\partial^2 T}{\partial y^2} + \frac{\partial \kappa}{\partial T} \left(\frac{\partial T}{\partial x} \right)^2 + \frac{\partial \kappa}{\partial T} \left(\frac{\partial T}{\partial y} \right)^2 + \frac{1}{\mu^2 \sigma} \left[\left(\frac{\partial B}{\partial x} \right)^2 + \left(\frac{\partial B}{\partial y} \right)^2 \right] - E_L. \quad (5)$$

The term E_L which appears in this equation represents the energy absorbed per unit volume and time by the solid during melting. A specific representation for this quantity will be discussed subsequently. The remaining terms are fairly obvious except perhaps for the terms enclosed in the square brackets. However, if we use equations (1)-(3) that contribution can just be recognized as J^2/σ and thus accounts for resistive heating in the armature and rails.

In the rails, where melting is neglected, we have $E_L = 0$ and $v = -v_p$; in the armature, we have $v = 0$.

Equations (4) and (5) represent two coupled, nonlinear partial differential equations which must be solved to determine the time evolution of the induction field and the temperature. Once these quantities have been obtained, other variables of interest such as the current density and electromagnetic forces within the rail-armature system can be obtained in a straightforward manner.

2.2 Boundary Conditions. The solution of equations (4) and (5) requires implementation of certain boundary conditions. It is assumed in our analysis that there is no heat transfer from the railgun into the surrounding air. Consequently, at each conductor surface we require that

$$\hat{n} \cdot \nabla T = 0 \quad (6)$$

where \hat{n} is the unit vector at the surface (pointing into the conductor). Such a condition also applies along the centerline from symmetry.

Boundary conditions on the magnetic induction can be determined at most surfaces from Ampere's law. If we denote by j the total current per unit rail height, we must have that

$$B = \mu j \quad \text{on } S_1 \text{ and } S_2 \quad (7)$$

and

$$B = 0 \quad \text{on } S_4, S_5, \text{ and } S_6. \quad (8)$$

Along the centerline, we have from symmetry,

$$\frac{\partial B}{\partial y} = 0 \quad \text{on } S_7, \quad (9)$$

and along the left-hand end of the rail, we assume that current enters parallel to the x axis so that

$$\frac{\partial B}{\partial x} = 0 \quad \text{on } S_3. \quad (10)$$

For this last assumption to be valid, it is necessary that the breech end of the rail be sufficiently far away from the armature that the current distribution at the breech is not affected by the armature motion.

In general, the rails and armature are assumed to be composed of different materials so that $\partial B/\partial y$ and $\partial T/\partial y$ are not continuous across the interface. The appropriate jump conditions in these variables can be determined by integrating equations (4) and (5) across the boundary of assumed thickness ϵ and then taking the limit as ϵ tends to zero. One finds

$$\left[\frac{1}{\sigma} \frac{\partial B}{\partial y} \right] = 0 \quad \text{at the interface} \quad (11)$$

and

$$\left[\kappa \frac{\partial T}{\partial Y} \right] = 0 \quad \text{at the interface} \quad (12)$$

where the brackets (here only) denote the change in the quantity enclosed as the interface is crossed.

2.3 Representation of the Heat Absorbed During Melting. For most pure metals, melting takes place at a reasonably well-defined temperature T_m . In such a case, it is customary [see, e. g., Powell (1983)] to represent the term E_L in equation (5) as

$$E_L = \rho L \delta(T - T_m) \frac{\partial T}{\partial t}, \quad (13)$$

where L represents the latent heat of fusion and δ is a delta function. The singular nature of the delta function assures that energy L is absorbed by the solid at temperature T_m to produce an equivalent amount of liquid without any change in temperature.

For typical armature alloys, however, melting occurs over a small range in temperatures and, in that case, equation (13) must be replaced by the more general expression

$$E_L = \rho L F(T) \frac{\partial T}{\partial t}. \quad (14)$$

The function $F(T)$ corresponds to the amount of liquid produced per unit rise in temperature of the solid-liquid mixture. For most materials $F(T)$ is determined from phase diagrams, but this information is not known for most armature materials. It is generally known, however, that melting is initiated at some approximate temperature T_i and is completed by some final temperature T_f . To approximate the physical situation, we will assume that $F(T)$ can be represented by a “coarse-grained” delta function which we represent as

$$F(T) = \frac{1}{\pi} \frac{\epsilon}{(T - T_{av})^2 + \epsilon^2}. \quad (15)$$

Here $T_{av} = (T_i + T_f)/2$ and ϵ is to be chosen so that the function is suitably peaked about T_{av} . This particular choice of the function $F(T)$ is, of course, not unique, but the representation does seem reasonable until more detailed information is known. It is furthermore possible to show that

$$\lim_{\varepsilon \rightarrow 0} F(T) = \delta(T - T_m). \quad (16)$$

As an example that will be used in our later analysis, we take $T_i = 750$ K, $T_f = 908$ K, and $\varepsilon = (T_f - T_i)/6$. We then obtain for $F(T)$ the function shown in Figure 3. It should be noted that $F(T_i) = F(T_f) \approx 0.1 F(T_{av})$ so that about 90% of the latent heat is absorbed in the relevant temperature range.

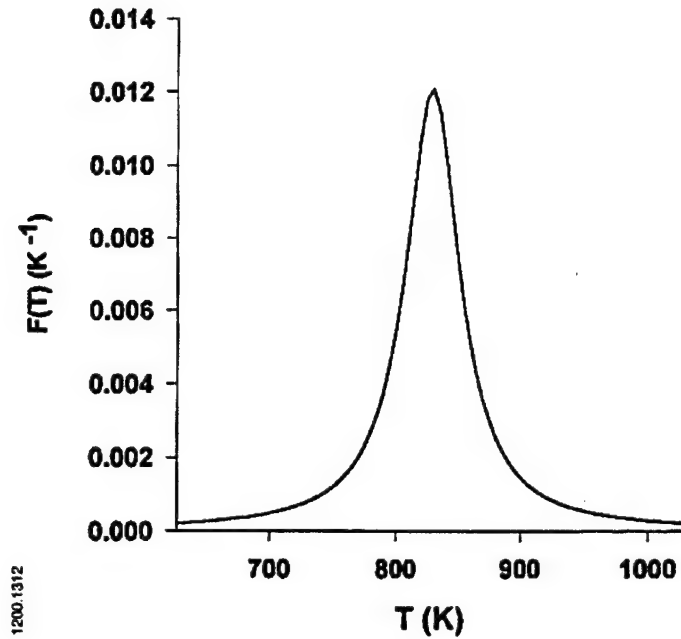


Figure 3. Function, $F(T)$, Depicting Amount of Melted Material Formed Per Unit Rise in Temperature.

2.4 Transformed Coordinates. Because armatures generally have irregular and complicated shapes, it is convenient to perform a coordinate transformation which maps the armature into a rectangular domain. Solutions of the pertinent differential equations are then carried out in this rectangular region, known as the computational space, and the resulting solutions then transformed back into the physical space of the armature. This procedure has a number of advantages, including easy implementation of the boundary conditions and extreme flexibility. It also provides a rather simple method by which grid spacing can be controlled. In

this section, we develop a general transformation for mapping an armature of arbitrary shape into a rectangular computational space, and obtain the transformed versions of equations (4) and (5). We then consider a situation in which the transformed coordinates satisfy Laplace's equation, and show that this restriction results in a significant simplification of the resulting equations. The analysis in this section is similar to that discussed by Hoffman (1989), although some modifications have been introduced and the application here is for the equations of electrodynamics rather than fluid dynamics.

We denote the coordinates in the actual physical space by x , y , and t and define a transformation to new coordinates ξ , η , and τ which define the computational space. Thus, we write

$$\begin{aligned}\xi &= \xi(x, y, t) \\ \eta &= \eta(x, y, t) \\ \tau &= t\end{aligned}\tag{17}$$

The partial derivatives which appear in equations (4) and (5) are then obtained in terms of the new variables by the chain rule. In particular, we have for any function F^*

$$\begin{aligned}F_x &= F_\xi \xi_x + F_\eta \eta_x \\ F_y &= F_\xi \xi_y + F_\eta \eta_y \\ F_t &= F_\tau + F_\xi \xi_t + F_\eta \eta_t\end{aligned}\tag{18}$$

for the first derivatives, and

$$\begin{aligned}F_{xx} &= F_\xi \xi_{xx} + F_\eta \eta_{xx} + \xi_x^2 F_{\xi\xi} + \eta_x^2 F_{\eta\eta} + 2\xi_x \eta_x F_{\xi\eta} \\ F_{yy} &= F_\xi \xi_{yy} + F_\eta \eta_{yy} + \xi_y^2 F_{\xi\xi} + \eta_y^2 F_{\eta\eta} + 2\xi_y \eta_y F_{\xi\eta} \\ F_{xy} &= F_\xi \xi_{xy} + F_\eta \eta_{xy} + \xi_x \xi_y F_{\xi\xi} + \eta_x \eta_y F_{\eta\eta} + (\xi_x \eta_y + \xi_y \eta_x) F_{\xi\eta}\end{aligned}\tag{19}$$

for the second derivatives.

* In this section and in Appendix A, subscripts are used to denote partial derivatives.

The results in equations (18) and (19) can now be substituted into equations (4) and (5) to produce the transformed equations. It is evident, however, that the results will still contain derivatives of the computational-space coordinates, ξ and η , with respect to the physical-space coordinates, x , y , and t . Consequently, before any progress can be made these derivatives must be expressed as derivatives of x and y with respect to ξ , η , and τ . The derivation of the pertinent relationships is actually fairly complicated and has been relegated to Appendix A. The results which are needed in the substitution are summarized as follows:

$$\begin{aligned}
 \xi_x &= Q y_\eta \\
 \eta_x &= -Q y_\xi \\
 \xi_y &= -Q x_\eta \\
 \eta_y &= Q x_\xi \\
 \xi_t &= Q(x_\eta y_\tau - y_\eta x_\tau) \\
 \eta_t &= Q(y_\xi x_\tau - x_\xi y_\tau),
 \end{aligned} \tag{20}$$

where Q is the Jacobian of the transformation, given by

$$Q = 1 / (y_\eta x_\xi - x_\eta y_\xi). \tag{21}$$

When the relevant substitutions are made in equations (4) and (5), there still remain terms that are multiplied by factors such as $(\xi_{xx} + \xi_{yy})$ and $(\eta_{xx} + \eta_{yy})$. Expressions for these second derivatives in terms of physical-space coordinates can also be obtained from results in Appendix A. However, some considerable simplification is obtained if we restrict ourselves to transformations in which ξ and η satisfy Laplace's equation. Consequently, we require

$$\begin{aligned}
 \xi_{xx} + \xi_{yy} &= 0 \\
 \eta_{xx} + \eta_{yy} &= 0.
 \end{aligned} \tag{22}$$

Some additional rationale for choosing a transformation of this type has been discussed in detail by Hoffman (1989).

We now substitute the preceding results into equations (4) and (5) and obtain for the governing equations in transformed coordinates

$$\begin{aligned} & \mu\sigma[B_\tau + Q(x_\eta y_\tau - y_\eta x_\tau)B_\xi + Q(y_\xi x_\tau - x_\xi y_\tau)B_\eta] + \mu\sigma Qv(y_\eta B_\xi - y_\xi B_\eta) = \\ & Q^2(x_\eta^2 + y_\eta^2)B_{\xi\xi} + Q^2(x_\xi^2 + y_\xi^2)B_{\eta\eta} - 2Q^2(x_\xi x_\eta + y_\xi y_\eta)B_{\xi\eta} - \\ & \frac{Q^2\sigma_\tau}{\sigma}[(x_\eta^2 + y_\eta^2)T_\xi B_\xi + (x_\xi^2 + y_\xi^2)T_\eta B_\eta - (x_\xi x_\eta + y_\xi y_\eta)T_\xi B_\eta - (x_\xi x_\eta + y_\xi y_\eta)T_\eta B_\xi] \end{aligned} \quad (23)$$

and

$$\begin{aligned} & \rho[C + LF(T)]T_\tau + Q(x_\eta y_\tau - y_\eta x_\tau)T_\xi + Q(y_\xi x_\tau - x_\xi y_\tau)T_\eta + \rho CvQ(y_\eta T_\xi - y_\xi T_\eta) = \\ & \kappa Q^2[(x_\eta^2 + y_\eta^2)T_{\xi\xi} + (x_\xi^2 + y_\xi^2)T_{\eta\eta} - 2(x_\xi x_\eta + y_\xi y_\eta)T_{\xi\eta}] + \\ & \kappa_\tau Q^2[(x_\eta^2 + y_\eta^2)T_\xi^2 + (x_\xi^2 + y_\xi^2)T_\eta^2 - 2(x_\xi x_\eta + y_\xi y_\eta)T_\xi T_\eta] + \\ & \frac{Q^2}{\mu^2\sigma}[(x_\eta^2 + y_\eta^2)B_\xi^2 + (x_\xi^2 + y_\xi^2)B_\eta^2 - 2(x_\xi x_\eta + y_\xi y_\eta)B_\xi B_\eta] \end{aligned} \quad (24)$$

As is customary in these types of transformations, the resulting equations are considerably more complicated than they were in the original coordinates. Nonetheless, the advantages gained with the transformation far outweigh the inconvenience of having to solve more complicated equations.

There now remains the necessity of solving equations (22) to determine the transformation. These equations must be solved in the rectangular computational space and, consequently, it is necessary to represent them in terms of various derivatives of x and y with respect to ξ and η rather than in the opposite manner. From the results in Appendix A, equations (A-12) and (A-13), we find that equations (22) become

$$\begin{aligned}
(x_\eta^2 + y_\eta^2)x_{\xi\xi} + (x_\xi^2 + y_\xi^2)x_{\eta\eta} - 2(x_\xi x_\eta + y_\xi y_\eta)x_{\xi\eta} &= 0 \\
(x_\eta^2 + y_\eta^2)y_{\xi\xi} + (x_\xi^2 + y_\xi^2)y_{\eta\eta} - 2(x_\xi x_\eta + y_\xi y_\eta)y_{\xi\eta} &= 0.
\end{aligned} \tag{25}$$

The procedure to be applied in the numerical solution of the foregoing equations can then be described as follows. A rectangular grid, described by coordinates ξ and η , is specified. The mapping into physical space is undertaken by specifying the mapping of certain points (x,y) on the boundaries of the physical domain by, for example, an algebraic transformation. Other points within the interior of the physical domain are determined by solving equations (25). Once x and y are known as functions of the computational-space coordinates, the results are used in equations (23) and (24) to determine B and T as functions of ξ , η , and τ . Since the mapping between (x,y) and (ξ,η) is one-to-one, the values of these variables are therefore known at all points within the physical space.

The numerical technique that is applied to solve equations (23) and (24) as well as equations (25) has been described in our earlier work (Powell, Walbert, and Zielinski 1993), and will not be discussed in detail here. In brief, all derivatives are represented by standard finite differences and the resulting nonlinear equations solved by iteration (Ames 1997). Specific grids employed will be discussed in the following section. Typically, a time step of 50-100 ns proves to be satisfactory.

3. ANALYSIS OF SCALED MCA 1.0.5

We now discuss a calculation that we have undertaken with this newly developed code to analyze the scaled version of the armature MCA 1.0.5. Our representation of this armature is shown in Figure 2. The rails were assumed to be composed of copper and the armature fabricated from aluminum alloy 7075. Material properties used in the calculation are presented

as a function of temperature in Appendix B. The absorption of the latent heat of aluminum was represented as in the example discussed earlier. In particular, melting was assumed to be initiated at $T_i = 750$ K and completed at $T_f = 908$ K, and L was taken to be 4.0×10^5 J/kg. The functional form for $F(T)$ is that indicated in equation (15).

3.1 Geometry and Transformation Coordinates. To effect the transformation to computational space, we chose the rectangular domain and accompanying grid shown in Figure 4. The figure actually depicts only a part of the grid since we have plotted only every third interior point in the ξ direction and every third one in the η direction. Consequently, there were nearly an order of magnitude more grid points used than are shown in the figure. Note that the rectangular grid extends for a distance ℓ_a of approximately 16.5 mm along the x axis, and this distance is equal to the length of the armature at the interface where $y = 7.5$ mm (see Figure 2). Grids similar to that shown in the figure have been used in our earlier calculations for armatures composed of rectangular regions.

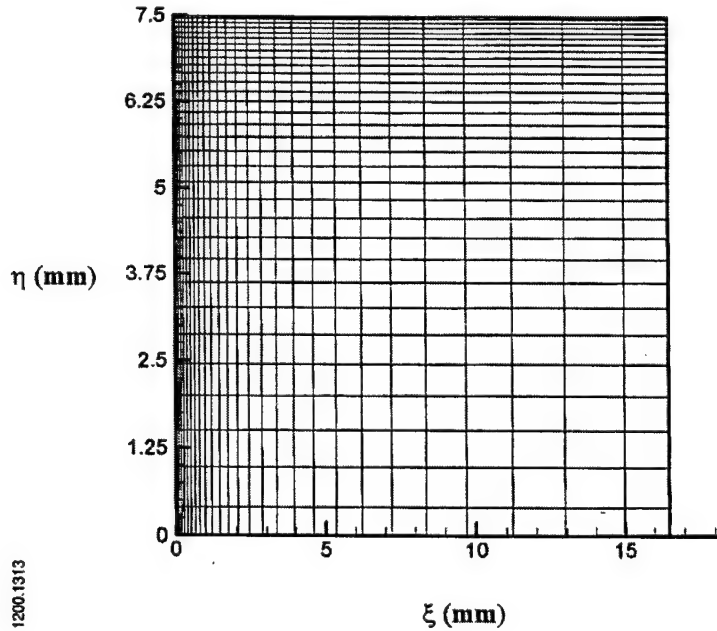
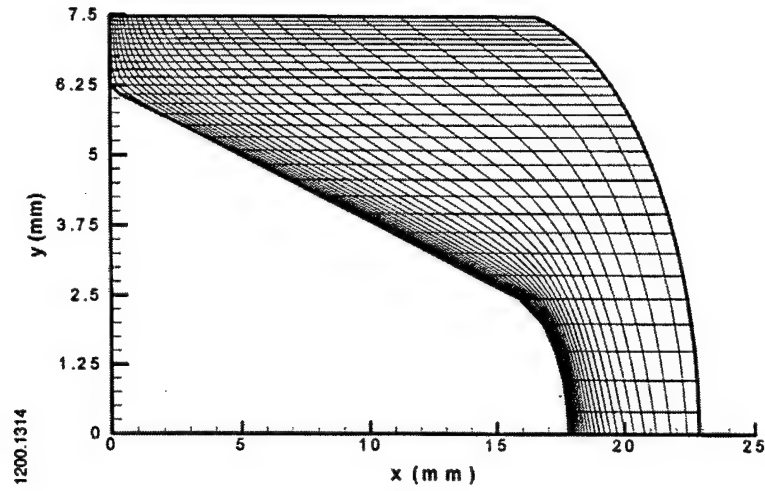


Figure 4. Rectangular Grid for the Computational Domain of the Armature.

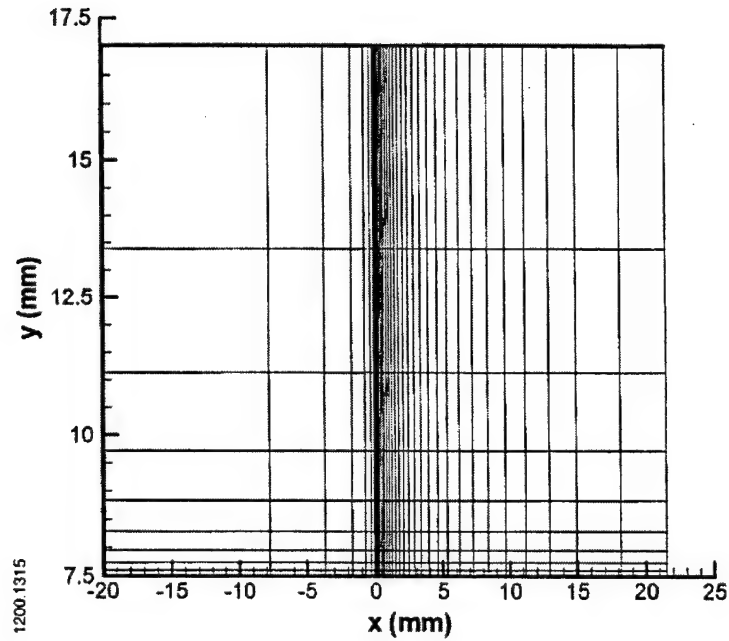
It is then necessary to map the physical space (Figure 2) into the rectangular computational space (Figure 4). One possible transformation can be defined by the algebraic result

$$\begin{aligned} x &= \frac{s_2(y) - s_1(y)}{\ell_a} \xi + s_1(y) \\ y &= \eta, \end{aligned} \tag{26}$$

where s_1 and s_2 represent the x coordinate of the front and back edge of the armature, respectively, at some given y coordinate. Although this transformation will not satisfy Laplace's equation, it can be used to specify the location of points on the boundary of the armature in physical space as well as provide an initial guess for the location of interior points. Once this initial guess has been made, equations (25) can be solved iteratively to determine the actual location of grid points on the interior of the physical domain. The solution of these equations has been obtained and produced the grid shown in Figure 5a, again with only every third interior point shown in each direction. Once the final physical-space grid had been obtained, the transformation metrics, $\partial x / \partial \xi$, $\partial x / \partial \eta$, $\partial y / \partial \xi$, and $\partial y / \partial \eta$, needed in the solution of equations (23) and (24), were also calculated.



(a)



(b)

Figure 5. Grid for (a) the Physical Domain of the Armature; and (b) the Rails.

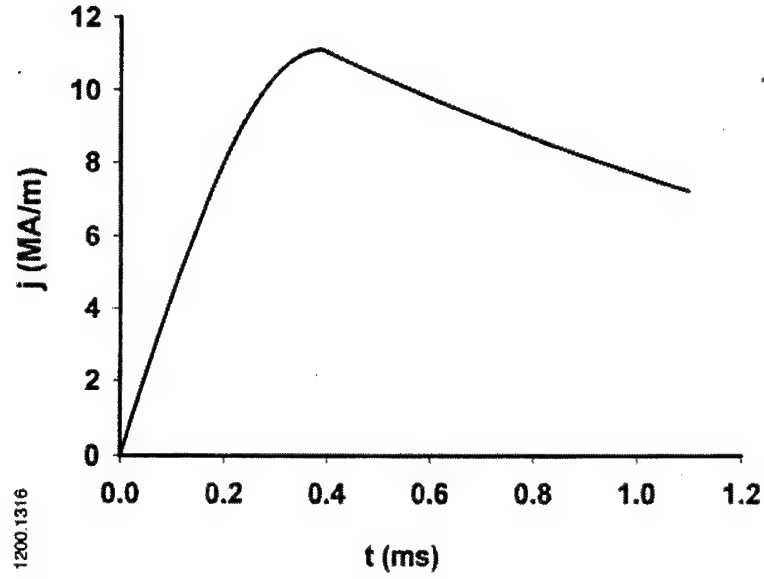
In the rails, a nonuniform rectangular grid was used similar to those which have been employed in our earlier calculations. A part of the rail, with accompanying grid, is shown in Figure 5b. Again, only every third interior point in each direction, is shown. In addition, only

the part of the rail extending approximately 2 cm to the left of the armature and the part extending approximately 0.5 cm to the right of the armature are plotted. The remaining part of the rail on the left had the uniform grid spacing of approximately 5 mm. On the right, the calculation was not extended farther than the point shown because the fields decay rapidly ahead of the armature. Along the interface, the grid points in the rail, in the computational space of the armature, and in the physical space of the armature are coincident.

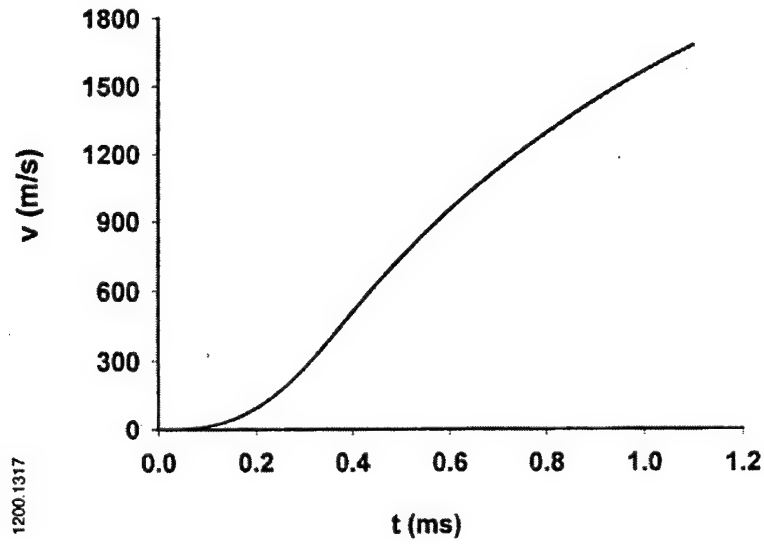
3.2 Input Current Versus Time. As has been pointed out previously, we have chosen to scale the experimental current versus time so that we obtained the correct velocity for an actual two-dimensional railgun with infinite rail height. The functional form of the current per unit rail height as a function of time was obtained from experiment and obeyed the relations

$$\begin{aligned} j &= j_0 \sin\left(\frac{\pi}{2t_p} t\right) & t < t_p \\ j &= j_0 e^{-(t-t_p)/t_2} & t \geq t_p, \end{aligned} \quad (27)$$

where the time constants t_p and t_2 were given by 390 μ s and 1650 μ s, respectively. We then calculated the amplitude j_0 so that the two-dimensional armature reached a velocity of about 1675 m/s in 1.1 ms, the nominal experimental result. The value obtained for j_0 was approximately 11.1 MA/m, about a factor of two smaller than the real, experimental peak value of approximately 20 MA/m. Graphs of the scaled $j(t)$ and the projectile velocity $v_p(t)$ are shown in Figure 6.



(a)



(b)

Figure 6. Time Dependence of (a) the Current Per Unit Rail Height; and (b) the Velocity.

3.3 Results of Calculations. The solution of equations (23) and (24) was carried out numerically and values of B and T were found as functions of both position and time in the armature and in the rails. Results will be presented in the form of graphs which indicate lines of

constant T (isotherms) as well as lines of constant B within the armature and rails. It can be proved from Maxwell's equations that current cannot cross lines of constant induction, so the constant B -field lines can also be inferred to represent current streamlines or the general path followed by the current. The results will be presented at two times: The first is at $400\ \mu\text{s}$, just subsequent to the time the current reaches peak value ($390\ \mu\text{s}$), and the second is at $1.1\ \text{ms}$, just prior to the time the projectile exits the bore.

Shown in Figure 7 are lines of constant induction at $400\ \mu\text{s}$. At this time, the velocity of the armature was about $512\ \text{m/s}$ and the current per unit rail height was about $11.1\ \text{MA/m}$. It is interesting to note that the current, which is initially confined only to the left-hand face of the armature, has essentially diffused throughout the entire armature by this time. It may also be noted that the gradient in the B -field along the armature-rail interface ($y = 7.5\ \text{mm}$) is highest at the left-hand side. This behavior occurs because of the velocity skin effect, a phenomenon which we have discussed in previous work. Essentially, the motion of the armature limits the amount of time available for current to diffuse into the rails during the time the armature is in contact with a given point on the rail surface. Consequently, current tends to be concentrated toward the back of the armature in the vicinity of the interface. While the effect is apparent in the figure, it is somewhat more obvious in rectangular armatures; in the cases studied here, there is substantial curvature of the field lines toward the breech simply because of the armature geometry.

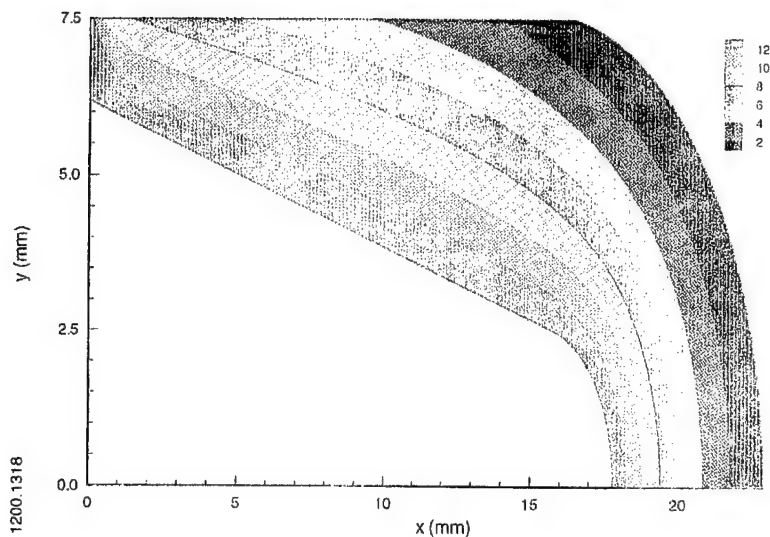


Figure 7. Lines of Constant Induction within the Armature at 400 μ s.

Isotherms at 400 μ s are shown in Figure 8. The maximum temperature in the armature is about 550 K, and the location of the maximum is on the left-hand side about 80 μ m below the interface. The substantial heating around this point is caused by the large current concentration resulting from the velocity skin effect. It is interesting, however, that the location of the maximum is somewhat removed from the interface. Presumably, this behavior can be attributed to conductive cooling at the interface, a phenomenon which occurs because the armature is moving and always encounters new, cold rail material. There is, consequently, a very steep temperature gradient in the armature toward the breech near the interface. There is also substantial heating on the breech side of the armature near the centerline where there is appreciable surface curvature (i. e., at the root radius). We have also noted this type of behavior in our previous work. In particular, current is expected to be concentrated in regions of the conductor where the surface curves through an angle of greater than 180 degrees (measured in the conductor). The resultant high current density then produces more significant heating than occurs along regions of the conductor that are fairly straight, and the amount of heating increases with increasing angle. Alternatively, regions in the conductor where the surface curves through

angles smaller than 180 degrees tend to carry small amounts of current and to be relatively cool. Thus, on the left-hand side of the armature at about $y = 6$ mm where such an angle is incurred, the temperature is somewhat lower than in the surrounding region. At no place in the armature has the incipient melt temperature of 750 K been reached at this time.

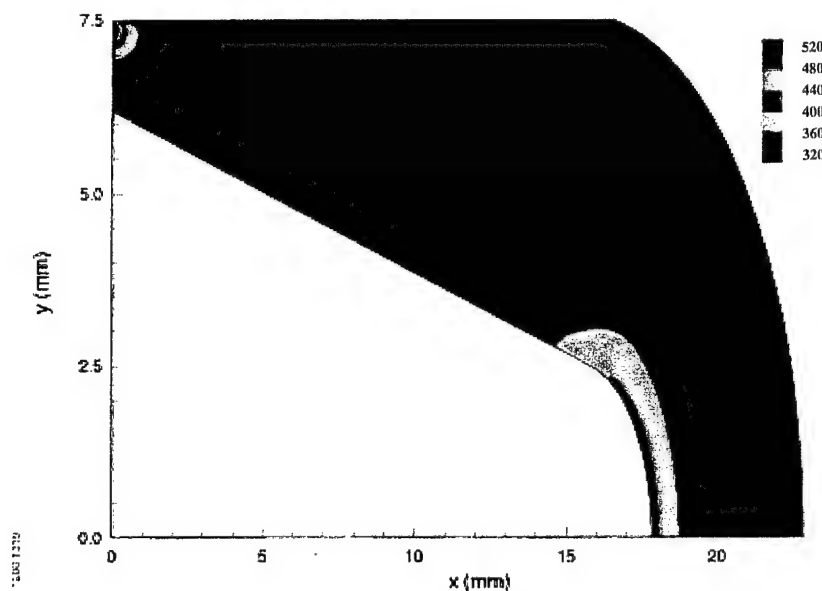


Figure 8. Isotherms within the Armature at 400 μ s.

Similar behavior is evident in the isotherms at 1.1 ms shown in Figure 9. At this time, the armature velocity has reached 1,675 m/s, the current per unit rail height has dropped to about 7.7 MA/m, and the projectile is just about to exit the gun. The maximum temperature is now about 1,100 K and the location of the maximum is about 175 μ m below the interface. Presumably, the maximum is at a value of y lower than that observed at 400 μ s because the higher velocity causes the armature to encounter cold rail material at a higher rate. There is a small region around the location of maximum temperature that has completely melted ($T > 908$ K), and a larger region that is undergoing incipient melt ($750 \text{ K} < T < 908 \text{ K}$).

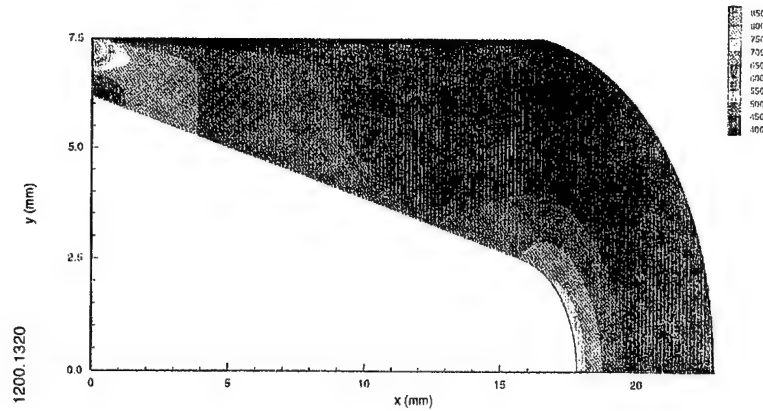


Figure 9. Isotherms within the Armature at 1100 μ s.

The extremely large temperature gradient in both the x and y directions near the interface corner can be seen more directly in Figure 10. In this figure, the temperature is plotted versus x for a short distance to the right and left of the corner along the interface (curve labelled I), just inside the armature (curve labelled A), and just inside the rails (curve labelled R). The "A" curve represents the temperature along the line $y = 7.325$ mm, and this line contains the grid point where the temperature is maximum (i. e., at $x = 0$). The curve labelled "R" was obtained in the rails along the $y = 7.684$ mm, or $184 \mu\text{m}$ above the interface. It is evident in the figure that there is very little heating in the rails beyond the interface, and this behavior is yet another manifestation of the velocity skin effect.

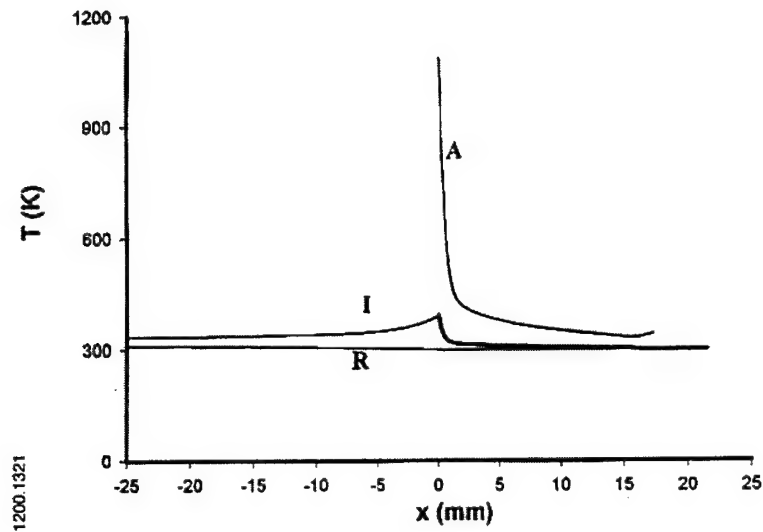


Figure 10. Temperature Versus x at Constant Values of y : A, Just Inside the Armature ($y = 7.325$ mm); I, Along the Interface ($y = 7.5$ mm); R, Just Inside the Rails ($y = 7.684$ mm).

As was indicated earlier, this particular armature has been under experimental study at the Army Research Laboratory. Experimental conditions were similar to those discussed in the calculation, except for the scaling of the current described before. It is of some interest to examine briefly results of the diagnostic measurements on the armature since these measurements provide a method for assessing its performance. Diagnostic measurements, described more fully elsewhere (Zielinski and Le 1996), included measurements of the surrounding electric and magnetic fields, the time rate of change of the launcher current, and magnitudes of the breech and muzzle voltages as a function of time. In addition, flash x-ray stations were used to visualize the armature after exit.

We present some of the data for one shot in this experimental study (Shot 6). A plot of the measured muzzle voltage is shown in Figure 11. The armature operated at less than 20 volts for most of the acceleration. A small transition to 30 volts is seen at 0.97 ms and lasts for nearly 50 μ s. The voltage resumes a 20 volt drop at 1.0 ms where it remains until exit at 1.1 ms. The rapid rise at 1.1 ms to 1800 volts is indicative of opening the inductive circuit (i.e., the railgun) with 200 kA flowing in the armature. The voltage measured at the muzzle can be used to assess

the performance of the armature. Typically, solid-armature performance is considered good when the muzzle voltage is less than 20 volts. The sudden rise to roughly 30 volts is indicative of one of the armature contacts transitioning to a low-ionized plasma state. This state can briefly oscillate between 20 and 30 volts and is often indicative of one armature contact skipping along the rail surface. A small patch of aluminum was observed on one rail surface after the shot, consistent with a loss of contact and the observed rise in muzzle voltage.

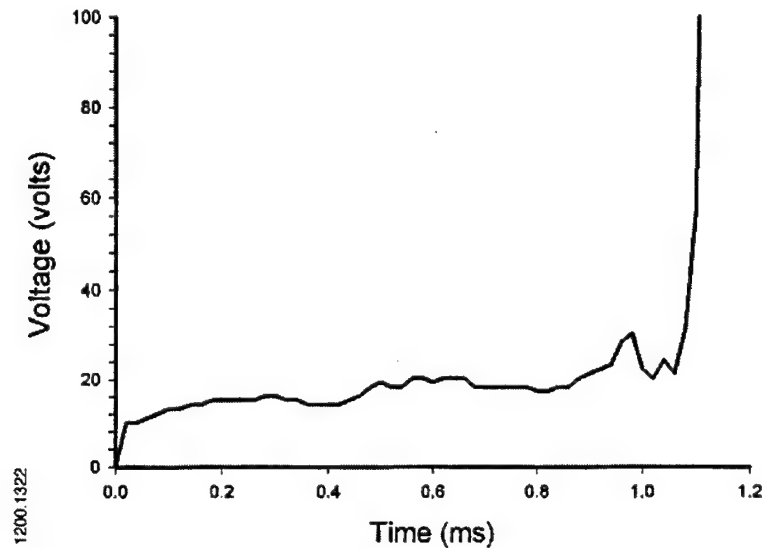


Figure 11. Measured Muzzle Voltage Versus Time.

Three flash x-ray images were also obtained a few meters downrange of the launcher. Photographs of the x-rays are shown in Figure 12. Parts a and b are from an orthogonal x-ray station, whereas c is from a single station slightly farther downrange. Since the x-rays are taken downrange of the muzzle and the armature is not aerodynamically stable, the armature is tumbling. In order to facilitate visualization of the armature in the x-ray images, there are also included in the figure illustrations of the armature with the same orientation as in the x-ray. The contact surfaces and root radius are not clearly visible in the images. However, it appears that there is no major loss of armature material at the contacts and at the root radius.

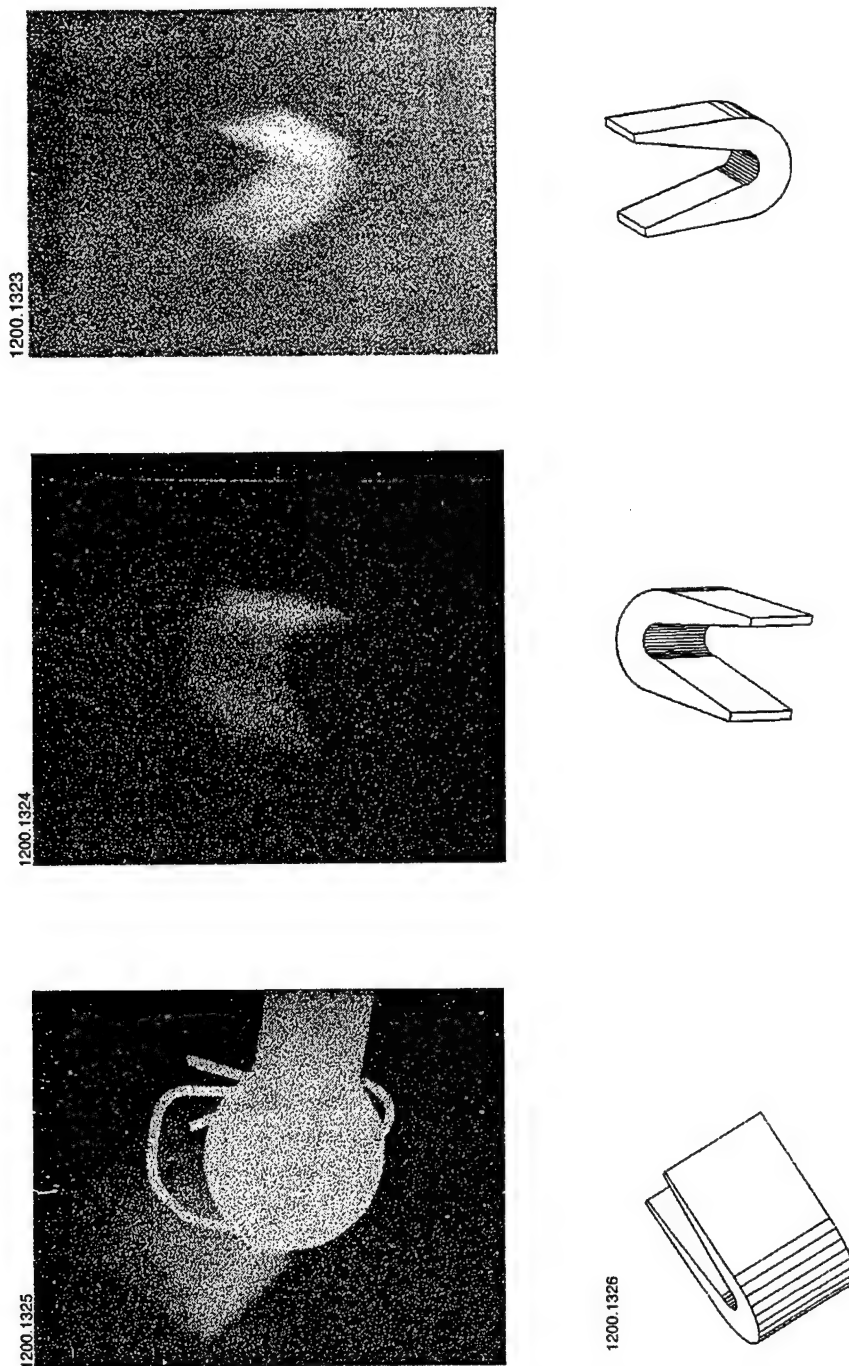


Figure 12. Flash X-ray Images of Armature Downrange of Launcher .

The x-ray images are consistent with calculations for temperature presented in Figure 9 in the sense that the calculations reveal no melting at the root radius and minimal melting at the trailing edge of the contact. Furthermore, the low voltage measured at the muzzle is consistent

with these same observations. This consistency is certainly not surprising since the current was scaled down as noted before. On the other hand, in previous tests with a tandem-contact armature, the x-rays clearly show signs of missing material from the contacts and the root radius (Zielinski and Hildenbrand 1997). Calculations corresponding to these tests were also performed in earlier work in which the current was scaled in the same manner described here. For that case the calculations indicated temperatures predicting that significant melting at the trailing edge of the contact and at the root radius occurred. On a lower-current test with the same tandem-contact design, the x-ray image showed negligible erosion at the contact and root radius. Similarly, the calculations for that test indicated minimum melting at these two locations.

4. ENTRAINMENT OF MELTED ARMATURE MATERIAL ON THE RAILS

There has been some speculation in recent years that melted armature material at the rail-armature interface could be entrained along the surface of the rails by viscous forces. If such an effect occurs, clearly there will arise a gap between the rails and armature at the interface, and this gap will move forward as additional melting takes place. Ultimately, it has been hypothesized, complete solid contact between the armature and rails will be lost and transitioning to a plasma in the interface will occur. We discuss in this section a one-dimensional model that has been developed to describe the propagation of the melt surface through the solid, describe some calculations that we have done in an effort to assess the importance of this effect, and give some indication of specific numerical calculations that would be advisable in the future. Most of the calculations described are preliminary and to some extent speculative and require further study.

The one-dimensional model is based on the assumptions that the material properties are constant, that the current is independent of time, and that the heat of fusion L is absorbed uniformly (i.e., as a step function) between values of temperature given by T_i and T_f . Although we have performed some numerical calculations for time-dependent problems, we will restrict

discussion here to steady-state conditions for which the governing equations can be solved analytically. If we denote the location of the melt front by $x = s$, then in a frame of reference fixed at the front, the equation governing heat transport becomes

$$-C_{eff} \rho \dot{s} \frac{\partial T}{\partial \xi} = \frac{J^2}{\sigma} + \kappa \frac{\partial^2 T}{\partial \xi^2}, \quad (28)$$

where $\xi = x - s$, \dot{s} is the speed with which the melt front moves, and C_{eff} denotes an effective specific heat. C_{eff} is given explicitly by

$$\begin{aligned} C_{eff} &= C & \text{for } \xi > \xi_i \\ C_{eff} &= C + \frac{L}{T_f - T_i} & \text{for } \xi < \xi_i, \end{aligned} \quad (29)$$

where ξ_i denotes the location at which $T = T_i$.

For a known value of $J^2(\xi)$, equation (28) can be solved for $\xi < \xi_i$ and for $\xi > \xi_i$, with integration constants as well as \dot{s} and ξ_i determined from boundary conditions at $\xi = 0$, $\xi = \infty$, and $\xi = \xi_i$. Results then yield the temperature profile to the right of the melt front. If only \dot{s} is of interest, however, it is somewhat simpler just to integrate equation (28) over the entire space to the right of the melt front and obtain for the velocity

$$\dot{s} = \frac{\int_0^\infty J^2 d\xi}{\rho \sigma [C(T_f - T_0) + L]}. \quad (30)$$

A very crude approximation for J can be obtained if we assume that melting occurs just at the interface between the armature and the rails, and that just inside the rails we have an approximate balance of field diffusion and convection. Thus, we have for $\xi > 0$

$$B(\xi) \cong \mu j e^{-\mu \sigma_R v_p \xi}. \quad (31)$$

In obtaining this equation we have assumed $\dot{s} \ll v_p$ and have denoted by σ_R the conductivity of the rails. (Unsubscripted variables always refer to properties of the armature in this section.) We

$$J = \mu j \sigma_R v_p e^{-\mu \sigma_R v_p \xi}. \quad (32)$$

now assume continuity of J across the interface and employ equation (2) to find

$$\dot{s} = \frac{\mu j^2 \sigma_R v_p}{2\sigma\rho[C(T_f - T_0) + L]}, \quad (33)$$

Substituting (32) into equation (30) and evaluating the integral yield for the melt velocity where T_0 is the ambient temperature.

Because of the crude approximation employed to determine J at the interface, we would expect equation (33) to similarly provide only a crude approximation for the melt velocity. It is interesting, however, that Woods (1996), in a better, two-dimensional model, has obtained the same value for the armature current density at the corner formed by the melt front and the rails. This value was obtained by separating variables in the field-transport equation, and then using physical arguments to approximate the separation constants. The expression for the melt velocity obtained by Woods was the same as that given in equation (33), except that Woods' result contains a second term which represents a small correction. Apparently, the correction term results from the consideration of heat conduction in the y direction.

As an aside, we should now indicate that Woods (1997) has criticized the use by Young and Hughes (1982) (and, consequently, by Parks, who adopted their model) of the boundary condition set forth in our equation (11). This condition essentially forces the tangential components of the electric field to be continuous across the interface, and then computes the appropriate values from Ohm's law. The condition was also assumed in the present calculations and, insofar as we are aware, has been assumed by other investigators of this and similar problems (see, e.g., Long 1986; Long 1987; Shankar et al. 1995; Rodger et al. 1991; Hsieh 1997). Presumably, Woods' objection arises because of an electric dipole layer in the interface, whose existence may preclude the continuity of $E_{\text{tangential}}$. We have not been able to estimate reliably the magnitude of this effect, especially relative to other effects that have been neglected, and thus have adopted equation (11) as have others. Woods' contention does, however, merit additional study.

In the analysis undertaken in the preceding section, we observed that there existed an extremely steep temperature gradient near the rail-armature interface (see Figure 10), and that the maximum temperature in the armature was actually located a small distance below the interface. This observation seems to suggest that melting also would occur below the surface, and would leave a small layer of unmelted material between the melt front and rail. The behavior does not necessarily invalidate the entrainment hypothesis, since the unmelted layer is probably too thin to be structurally stable and is swept onto the rail surface along with melted material. On the other hand, the occurrence of melting even this small distance below the surface may affect the speed with which the front propagates.

In an effort to examine this contention in greater detail, we have used numerical results from calculations undertaken with rectangular armatures (not previously discussed) to approximate the melt-wave speed. In these calculations, the current per unit rail height j was increased linearly from zero to 20 MA/m in 50 μs , and then held constant for the remainder of the calculation. At about 190 μs , when the projectile velocity was about 150 m/s, we observed that melting was about to occur at a point $(0, y_m)$, where y_m was about 125 μm below the

interface. From the numerical data, we then evaluated $\int_0^{\ell_a} J^2(\xi, y_m) d\xi$ and used the result in equation (30) to approximate \dot{s} . Material-property values were assumed to be given by the arithmetic average of values at $T = 300$ K and $T = 908$ K (see Appendix B). We obtained the value $\dot{s} \approx 10$ m/s. If we use instead, equation (33), under the assumption that melting occurs at the interface with the current density given by equation (32), then we obtain for the same material-property values, $\dot{s} \approx 55$ m/s. There appear to be two reasons for the discrepancy. First, the current density at $(0, y_m)$ is smaller than that at interface, as is the integral over J^2 discussed above. Second, even at the interface, equation (32) appears to provide an overestimate of the current density near the corner. We have noted this overestimate by comparing that prediction with both our numerical data and with analytic results of Long (1986, 1987), who carried forward the full, two-dimensional separation-of-variables solution of the governing equations.

We have also performed the exercise just described at later times when the projectile velocity was higher. At $300 \mu\text{s}$, for example, when $v_p \approx 250$ m/s, we found that the maximum temperature was slightly farther removed from the interface, and the integral over J^2 was only slightly higher than before. In consequence, the melt-front velocity was nearly the same as that at $190 \mu\text{s}$, namely, about 10 m/s. The result predicted by equation (33) at this time is about 90 m/s.

Clearly, these calculations can be considered only very crude. First, especially at early times, the current density even near the corner of the armature may not be well approximated by steady conditions. Second, the current density may be perturbed somewhat by the motion of the melt surface or the removal of melted material, and that effect is not accounted for in the calculations. It is also not accounted for in equation (32), since we assumed $\dot{s} \ll v_p$, but may be less important if melting occurs directly at the interface than if it occurs at some point below. We should point out incidentally that the condition $\dot{s} \ll v_p$ is not well satisfied *a posteriori* by the result obtained from equation (33), since \dot{s} is only about one-third of the armature speed. Presumably, the more correct treatment, in which \dot{s} is included in the relative velocity between the melt front and the rails, would lead to an even higher velocity of the melt front and a greater

discrepancy with the numerical results. Third, at late times, there will exist some curvature of the melt surface and that effect, not accounted for in any of the calculations so far, will likely affect the melt rate. Finally, in the numerical calculations discussed, the armature resistivity was assumed to vary with temperature (and hence time) and increased somewhat during the time of the calculation. For instance, at $190\ \mu\text{s}$, the resistivity at $(0, y_m)$ was about $2.7 \times 10^{-7}\ \text{Ohm-m}$, and had increased to about $3.3 \times 10^{-7}\ \text{Ohm-m}$ at $300\ \mu\text{s}$. If the melted material were actually removed in the calculations, then the resistivity at the melt front would remain constant in time.

Despite these many caveats, we do believe that the foregoing analysis is sufficient to indicate that equation (33) probably does overestimate the velocity of the melt front. Before any definite conclusions can be reached, however, detailed numerical calculations in which the melted material is removed should be performed. We believe that the model described here, with transformed coordinates, could provide the basis for such a calculation. In particular, we could employ a transformation such that the time-dependent shape of the armature, which results from the removal of completely melted material, was continuously mapped into a rectangular computational space. An algebraic transformation similar to that indicated in equation (26), but with s_1 depending on t as well as y , and s_2 given by ℓ_a , would probably be satisfactory. The value of s_1 would be determined by the farthest location of the melt front in the armature at any time, and unmelted material located between that point and the interface would be removed. That assumption would be consistent with the notion described earlier that unmelted material between the interface and the melt front is entrained along with the melted material on the rail surface.

5. SUMMARY AND CONCLUSIONS

We have developed a general formalism for mapping an armature of fairly arbitrary shape into a rectangular computational space, and have demonstrated that the use of these transformed coordinates greatly simplifies numerical calculations. The formalism has been used to analyze a scaled version of the armature MCA 1.0.5 in some detail. Temperature and induction fields as

functions of both space and time have been predicted, and the physical reasons for the behavior of the armature have been discussed. General conclusions reached as a result of the analysis were:

- (1) Complete diffusion of current occurs throughout the armature during the time of the calculation. This effect, not observed in previous armatures which we have investigated, can be ascribed to the judicious design and small size of the armature studied here.
- (2) The velocity skin effect is important and leads to high thermal loading near the trailing corner of the armature. Even though the current was scaled down considerably to undertake the two-dimensional calculation, melting was nonetheless observed near that corner. The location of this high-temperature region is below the interface a small distance.
- (3) Other locations in the armature where the temperature is high include regions where the angle measured in the conductor is greater than 180 degrees. Such a region occurs in this armature at the trailing edge near the center line.
- (4) The experimental assessment of armature contact performance suggests little melting both at the root radius and at the armature contact. Future experimental work will include an attempt to measure the surface temperature of the armature. Such a measurement would provide more meaningful, albeit qualitative, correlation between theory and experiment. In addition, there appears to be a number of mechanical interactions, such as initial preload on the contact and gouging, that can alter the contact performance. These effects are not included in the present calculations.

We have also performed some limited calculations concerning the entrainment of molten armature material on the rail surface, and compared results with a simpler analytic model. These calculations are preliminary at this point, but have indicated that the simpler model may overestimate the velocity with which the melt surface advances into the armature. Before any

definite conclusions are made, however, some additional calculations are necessary. In particular, calculations which account directly for removal of melted material, and which allow the solid layer between the melt front and the interface to be entrained along with the melted material, would be worthwhile. A description of the appropriate calculations has been provided.

ACKNOWLEDGMENTS

The authors wish to thank the Institute for Advanced Technology and, in particular, P. H. Sullivan and K. T. Hsieh for technical and financial support.

This work was supported by the U.S. Army Research Laboratory (ARL) under contract DAAA21-93-C-0101.

REFERENCES

- Ames, William F. *Numerical Methods for Partial Differential Equations*. New York: Academic, 1977, Chap. 5.
- Hsieh, K. T. "A Lagrangian Formulation for Mechanically, Thermally Coupled Electromagnetic Diffusive Processes with Moving Conductors." *IEEE Transactions on Magnetism*, vol. MAG-31, p. 604, 1995.
- Hsieh, K. T. personal communication, August 1997.
- Long, G. C. "Railgun Current Density Distributions." *IEEE Transactions on Magnetism*, vol. MAG-22, p. 1597, 1986.
- Long, G. C. "Fundamental Limits to the Velocity of Solid Armatures in Railguns." Doctoral Dissertation, University of Texas at Austin, Publication Number TD-35, 1987.
- Parks, P. B. "Current Melt-Wave Model for Transitioning Solid Armature." *Journal of Applied Physics*, vol. 67, p. 3511, 1990.
- Powell, J. D. and A. E. Zielinski. "Current and Heat Transport in the Solid-Armature Railgun." *IEEE Transactions on Magnetism*, vol. MAG-31, p. 645, 1995.

- Powell, J. D., D. J. Walbert, and A. E. Zielinski. "Two-Dimensional Model for Current and Heat Transport in Solid-Armature Railguns." ARL-TR-74, U. S. Army Research Laboratory, Aberdeen Proving Ground, MD, 1993.
- Price, J. H. and H. D. Yun. "Design and Testing of Integrated Metal Armature Sabots for Launch of Armor Penetrating Projectiles from Electric Guns." *IEEE Transactions on Magnetics*, vol. MAG-31, p. 219, January 1995.
- Rodger, D. and P. J. Leonard. "Alternative Schemes for Electromagnetic Modeling of Rail Guns at Speed Using Finite Elements." *Proceedings of the Third European Symposium on EML Technology*, London, England, 1991.
- Rodger, D., P. J. Leonard, and J. F. Eastman. "Modeling Electromagnetic Rail Launchers at Speed Using 3D Finite Elements." *IEEE Transactions on Magnetics*, vol. MAG-27, p. 314, 1991.
- Rodger, D., P. J. Leonard, J. F. Eastman, and S. P. Atkinson. "3D Finite Element Modeling of Electromagnetic Launchers." *Proceedings of the Second European Symposium on EML Technology*, ISL St. Louis, France, 1989.
- Shankar, V., S. Chakravarthy, W. F. Hall, D. Ota, and S. Ramakrishnan. "Accurate Electromagnetic Modeling of Rail Gun Launch Process." Final Contractor Report, Contract Number SC-0060-89-0009, Rockwell International Science Center, January 1995.
- Woods, L. C. "The Current Melt-Wave Model." *IEEE Transactions on Magnetics*, vol. MAG-33, p. 152, 1997.
- Young, F. J. and W. F. Hughes. "Rail and Armature Current Distributions in Electromagnetic Launchers." *IEEE Transactions on Magnetics*, vol. MAG-18, p. 33, 1982.
- Zielinski, A. and C. Le. "Preliminary Findings on Magnetic Shielding Effectiveness for Railgun Applications," *Proceedings of the 14th Electric Launcher Association (ELA) Meeting*, October 1996, San Diego CA.
- Zielinski, A. and D. Hildenbrand. "Observation and Simulation of Armature Contact Performance in the Cannon-Caliber Electromagnetic Gun." *IEEE Transactions on Magnetics*, vol. MAG-33, p. 157, 1997.

APPENDIX A:
TRANSFORMATION METRICS

The purpose of this appendix is to derive expressions for the partial derivatives of the computational-space coordinates with respect to physical-space coordinates or, in other words, the results contained in equation (20). We also obtain expressions for the second derivatives ξ_{xx} , ξ_{yy} , η_{xx} , and η_{yy} . These relationships are needed in the derivation of equations (25).

Consider equations (18) and (19) and write in matrix form as

$$\begin{bmatrix} F_x \\ F_y \\ F_t \\ F_{xx} \\ F_{yy} \\ F_{xy} \end{bmatrix} = \begin{bmatrix} \xi_x & \eta_x & 0 & 0 & 0 & 0 \\ \xi_y & \eta_y & 0 & 0 & 0 & 0 \\ \xi_t & \eta_t & 1 & 0 & 0 & 0 \\ \xi_{xx} & \eta_{xx} & 0 & \xi_x^2 & \eta_x^2 & 2\xi_x\eta_x \\ \xi_{yy} & \eta_{yy} & 0 & \xi_y^2 & \eta_y^2 & 2\xi_y\eta_y \\ \xi_{xy} & \eta_{xy} & 0 & \xi_x\xi_y & \eta_x\eta_y & \xi_x\eta_y + \xi_y\eta_x \end{bmatrix} \begin{bmatrix} F_\xi \\ F_\eta \\ F_\tau \\ F_{\xi\xi} \\ F_{\eta\eta} \\ F_{\xi\eta} \end{bmatrix}, \quad (\text{A-1})$$

or symbolically as

$$\mathbf{F}_1 = \mathbf{A} \mathbf{F}_2, \quad (\text{A-2})$$

where \mathbf{F}_1 and \mathbf{F}_2 are column vectors and \mathbf{A} the 6 x 6 matrix. It is apparent that a similar equation could be written by interchanging the roles of the independent and dependent variables to produce

$$\mathbf{F}_2 = \mathbf{B} \mathbf{F}_1, \quad (\text{A-3})$$

where **B** is a matrix similar to **A** but with the interchanges: $x \rightarrow \xi$, $y \rightarrow \eta$, $\xi \rightarrow x$, $\eta \rightarrow y$, and $t \rightarrow \tau$. Consequently, we must have

$$\mathbf{A} \mathbf{B} = \mathbf{I} \quad (\text{A-4})$$

where **I** is the identity matrix.

Nontrivial results obtained by multiplying rows 1 and 2 of **A** with columns of **B** produce

$$\begin{aligned} \xi_x x_\xi + \eta_x x_\eta &= 1 \\ \xi_x y_\xi + \eta_x y_\eta &= 0 \\ \xi_y x_\xi + \eta_y x_\eta &= 0 \\ \xi_y y_\xi + \eta_y y_\eta &= 1. \end{aligned} \quad (\text{A-5})$$

These equations can now be solved by successive elimination to yield

$$\begin{aligned} \xi_x &= Q y_\eta \\ \eta_x &= -Q y_\xi \\ \xi_y &= -Q x_\eta \\ \eta_y &= Q x_\xi \end{aligned} \quad (\text{A-6})$$

where Q is given by

$$Q = \frac{1}{y_\eta x_\xi - x_\eta y_\xi}. \quad (\text{A-7})$$

Similarly, nontrivial results obtained by multiplying row 3 of **A** by columns of **B** are

$$\begin{aligned}\xi_t x_\xi + \eta_t x_\eta + x_\tau &= 0 \\ \xi_t y_\xi + \eta_t y_\eta + y_\tau &= 0\end{aligned}\tag{A-8}$$

whence

$$\begin{aligned}\eta_t &= Q(y_\xi x_\tau - x_\xi y_\tau) \\ \xi_t &= Q(x_\eta y_\tau - y_\eta x_\tau)\end{aligned}\tag{A-9}$$

The remaining nontrivial results obtained from multiplying **A** and **B** are the following six equations

$$\begin{aligned}x_\xi \xi_{xx} + x_\eta \eta_{xx} + \xi_x^2 x_{\xi\xi} + \eta_x^2 x_{\eta\eta} + 2\xi_x \eta_x x_{\xi\eta} &= 0 \\ y_\xi \xi_{xx} + y_\eta \eta_{xx} + \xi_x^2 y_{\xi\xi} + \eta_x^2 y_{\eta\eta} + 2\xi_x \eta_x y_{\xi\eta} &= 0 \\ x_\xi \xi_{yy} + x_\eta \eta_{yy} + \xi_y^2 x_{\xi\xi} + \eta_y^2 x_{\eta\eta} + 2\xi_y \eta_y x_{\xi\eta} &= 0 \\ y_\xi \xi_{yy} + y_\eta \eta_{yy} + \xi_y^2 y_{\xi\xi} + \eta_y^2 y_{\eta\eta} + 2\xi_y \eta_y y_{\xi\eta} &= 0 \\ x_\xi \xi_{xy} + x_\eta \eta_{xy} + \xi_x \xi_y x_{\xi\xi} + \eta_x \eta_y x_{\eta\eta} + (\xi_x \eta_y + \xi_y \eta_x) x_{\xi\eta} &= 0 \\ y_\xi \xi_{xy} + y_\eta \eta_{xy} + \xi_x \xi_y y_{\xi\xi} + \eta_x \eta_y y_{\eta\eta} + (\xi_x \eta_y + \xi_y \eta_x) x_{\xi\eta} &= 0.\end{aligned}\tag{A-10}$$

These results can now presumably be used to determine the second derivatives ξ_{xx} , ξ_{yy} , ξ_{xy} , η_{xx} , η_{yy} , and η_{xy} . However, as indicated before, a judicious choice of the transformation can preclude our actually having to solve the equations. For the special case which ξ and η satisfy Laplace's equations, we write the relation as

$$x_{\xi} \xi_{xx} + x_{\xi} \xi_{yy} + x_{\eta} \eta_{xx} + x_{\eta} \eta_{yy} = 0, \quad (\text{A-11})$$

and use the results above in equation (A-10) to obtain

$$(x_{\eta}^2 + y_{\eta}^2)x_{\xi\xi} + (x_{\xi}^2 + y_{\xi}^2)x_{\eta\eta} - 2(y_{\xi}y_{\eta} + x_{\xi}x_{\eta})x_{\xi\eta} = 0, \quad (\text{A-12})$$

for the appropriate governing equation in computational space. If, furthermore, we write an equation similar to (A-11), but with x_{ξ} replaced by y_{ξ} and x_{η} replaced by y_{η} , we obtain

$$(x_{\eta}^2 + y_{\eta}^2)y_{\xi\xi} + (x_{\xi}^2 + y_{\xi}^2)y_{\eta\eta} - 2(y_{\xi}y_{\eta} + x_{\xi}x_{\eta})y_{\xi\eta} = 0. \quad (\text{A-13})$$

APPENDIX B:

MATERIAL PROPERTIES

Material properties used in this analysis have been obtained from curve fits for copper and aluminum worked out by Zielinski. In those fits, it was assumed that the specific heat C , the resistivity η_r , the thermal conductivity κ , and the density ρ could be represented as linear functions of the temperature. Consequently, for any property F , we have

$$F = \alpha T + \beta.$$

Values of α and β for solid copper as well as solid and liquid aluminum are shown in Table B-1. All properties are expressed in MKS units.

Table B-1. Values of Coefficients Employed in Data for Copper and Aluminum

	Cu (CDA 110)		Al (7075)			
	Solid		Solid		Liquid	
Property	α	β	α	β	α	β
C	0.1	360.0	0.705	645.0	0	1302.0
η_r	7.81×10^{-11}	-5.42×10^{-9}	1.36×10^{-10}	1.42×10^{-8}	1.33×10^{-10}	1.51×10^{-7}
κ	-7.87×10^{-2}	412.0	-6.92×10^{-2}	247.0	0	93.0
ρ	-0.58	9125.0	-0.5	2851.0	0	2294.0

For aluminum, solid properties were used for values of temperature less than T_i , which was taken to be 750 K, and liquid properties were used above T_f , taken to be 908 K. At intermediate values of T , i. e., for a solid-liquid-mixture, the property in question was scaled linearly with temperature between the value for the solid at T_i and the value for the liquid at T_f . The only additional property needed in the analysis is the heat of fusion of aluminum, given by $L = 4.0 \times 10^5$ J/kg. The melting temperature of copper is about 1350 K, a value considerably higher than the maximum temperature reached anywhere in the rail in any of our calculations.

Distribution List

Administrator
Defense Technical Information Center
Attn: DTIC-DDA
8725 John J. Kingman Road,
Ste 0944
Ft. Belvoir, VA 22060-6218

Dr. George Chryssomallis
Science Applications International Corp.
3800 W. 80th St., Suite 1090
Bloomington, MN 55431

Mr. Dennis Ladd
COMMANDER, TACOM-ARDEC
ATTN: AMSTA-AR-FSP-E / Dennis Ladd
Bldg. 354
Picatinny Arsenal, NJ 07806-5000

Director
US Army Research Lab
ATTN: AMSRL OP SD TA
2800 Powder Mill Road
Adelphi, MD 20783-1145

Kathy Cominos
Office of the Assistant Secretary
of the Army (RDA)
Deputy Asst. Secretary of the
Army for Research & Technology
The Pentagon, Room 3E374
Washington, DC 20310-0103

Dr. Ingo W. May
Office of the Director
Army Research Laboratory
ATTN: AMSRL -WT
Army Research Laboratory
Aberdeen Prvg Grd, MD 20115-5066

Director
US Army Research Lab
ATTN: AMSRL OP SD TL
2800 Powder Mill Road
Adelphi, MD 20783-1145

Dan Dakin
Science Applications International Corp.
2000 Powell St., Suite 1090
Emeryville, CA 94608

Dr. John Powell
U.S. Army Research Laboratory
Attn: AMSRL-WT-WD
Bldg. 120
Aberdeen Prvg Grd, MD 21005-5066

Director
US Army Research Lab
ATTN: AMSRL OP SD TP
2800 Powder Mill Road
Adelphi, MD 20783-1145

Dr. Thaddeus Gora
U.S. Army Armament Research,
Development and Engineering Center
Attn: AMSTA-AR-FS Bldg. 94
Picatinny Arsenal, NJ 07806-5000

Bob Schlenner
U.S. Army Armament Research,
Development and Engineering Center
Attn: AMSTA-AR-CCL
Bldg. 65N
Picatinny Arsenal, NJ 07806-5000

Army Research Laboratory
AMSRL-CI-LP
Technical Library 305
Aberdeen Prvg Grd, MD 21005-5066

Dr. Robert Guenther
Army Research Office
P.O. Box 12211
Research Triangle Park, NC 27709-2211

Dr. Edward M. Schmidt
U.S. Army Research Laboratory
Attn: AMSRL-WT-P
Aberdeen Prvg Grd, MD 21005-5066

Dr. John P. Barber
IAP Research, Incorporated
2763 Culver Avenue
Dayton, OH 45429-3723

Mr. Albert Horst
Chief, Propulsion and Flight Division
Army Research Laboratory
ATTN: AMSRL -WT-P
Army Research Laboratory
Aberdeen Prvg Grd, MD 20115-5066

Robert J. Taylor
Lockheed Martin Vought Systems
M/S: WT-21
P.O. Box 650003
Dallas, TX 75265-0003

Dr. Bruce Burns
U.S. Army Research Laboratory
Attn: AMSRL-WT-PD
Bldg. 390
Aberdeen Prvg Grd, MD 21005-5066

Dr. Keith A. Jamison
Science Applications International Corp.
1247-B N. Eglin Parkway
P. O. Box 126
Shalimar, FL 32579

Alex Zielinski
U.S. Army Research Laboratory
AMSRL-WT-PB, B390, RM 212
Aberdeen Prvg Grd, MD 21005-5066

Distribution List

Raymond C. Zowarka
Center for Electromechanics
The University of Texas at Austin
Pickle Research Campus
EME 13, C R 7000
Austin, TX 78712